Computers and Structures 292 (2024) 107241

Contents lists available at ScienceDirect

Computers and Structures

journal homepage: www.elsevier.com/locate/compstruc

On modeling the *in vivo* ventricular passive mechanical behavior from *in vitro* experimental properties in porcine hearts

Nicolás Laita [a], Ricardo M. Rosales [a,b], Ming Wu [c], Piet Claus [c], Stefan Janssens [c], Miguel Ángel Martínez [a,b], Manuel Doblaré [a,b,*], Estefanía Peña [a,b]

[a] Aragon Institute of Engineering Research (I3A), University of Zaragoza, Spain
[b] Biomedical Research Networking Center in Bioengineering, Biomaterials and Nanomedicine (CIBER-BBN), Spain
[c] Department of Cardiovascular Sciences, University of Leuven, Belgium

ARTICLE INFO

Keywords:
Cardiac tissue
Myocardial mechanical behavior
Patient specific
Porcine heart
In vivo imaging
In vitro tests
Inverse approach

ABSTRACT

Myocardium passive mechanical response has been a major topic of study for decades due to its major impact on cardiac physiology. Here, we propose a novel modeling methodology that integrates both *in vivo* and *in vitro* data to estimate the tissue mechanical parameters for a particular orthotropic hyperelastic model as those proposed by Costa and by Holzapfel & Ogden, although it can be easily extended to any other. *In vitro* biaxial and triaxial shear extension tests were conducted in biopsied samples and *in vivo* pressure-volume recordings were obtained. Left ventricle (LV) geometry was reconstructed using magnetic resonance imaging (MRI) and pressure gradients during ventricular inflation were recorded with the Catheter Conductance Method (CCM). Finally, a Finite Element (FE) *in vivo* LV model was implemented to get the material model parameters using an inverse approach that uses a minimization process combining both the *in vivo* and *in vitro* available data. Our results demonstrate that the parameters obtained solely from *in vitro* testing (IVT), or from *in vivo* passive inflation (IVV) do not provide satisfactory fits for both responses simultaneously ($R^{2^{tests}}_{IVT} = 0.977, R^{2^{PV}}_{IVT} = 0.697$ and $R^{2^{tests}}_{IVV} = 0.687, R^{2^{PV}}_{IVV} = 0.995$). On the contrary, the proposed combined *in vitro* & *in vivo* optimization process (MIN) converges to a solution that effectively captures both the *in vivo* and *in vitro* behaviors ($R^{2^{tests}}_{MIN} = 0.815, R^{2^{PV}}_{MIN} = 0.992$). Thus, this novel combined approach offers a comprehensive framework for accurately characterizing myocardial mechanical behavior. The obtained parameters can serve as a basis for further cardiac simulations and contribute to a better understanding of cardiac mechanics and function.

1. Introduction

Myocardium mechanics has been a major focus of study for decades due to its major impact on cardiac physiology. Myocardium passive mechanical properties are of great importance in the cyclic function of the heart and in many cardiac pathologies such as diastolic heart failure or myocardial infarction [1,2]. Computational modeling has emerged in recent years as a powerful tool for the analysis of cardiac function and to develop novel devices and therapies [3]. In this context, obtaining realistic mechanical experimental properties for the myocardial tissue, as well as developing robust constitutive models is of vital importance to get reliable simulations.

The anatomic structure of cardiac tissue has been widely studied [4–7]. It is composed of three different layers: two thin membranes, the endocardium on the inside and the epicardium on the outside, and the internal myocardium, which comprises the main part of the heart's wall. As introduced by LeGrice [5], the myocardium presents a well-structured three-dimensional muscular fibers distribution in which the cardiomyocytes are arranged into parallel sheets separated by extensive cleavage planes, which are interconnected by collagenous fibers. In a simplified form, the muscular sheets are arranged along the radial direction, with the cardiomyocytes oriented parallel to the epicardial surface. This structure defines three main directions that characterize the mechanical behavior of the myocardium: the one of the muscle fibers (f), the sheet in-plane direction (s), and the normal to the cleavage planes (n).

Due to this very specific 3D structure, the cardiac muscle presents a highly non-linear anisotropic mechanical behavior. The publications to

* Corresponding author.
E-mail address: mdoblare@unizar.es (M. Doblaré).

https://doi.org/10.1016/j.compstruc.2023.107241
Received 15 July 2023; Accepted 17 November 2023
Available online 2 December 2023
0045-7949/© 2023 The Authors. Published by Elsevier Ltd. This is an open access article under the CC BY-NC-ND license (http://creativecommons.org/licenses/by-nc-nd/4.0/).

date have used several passive heterogeneous hyperelastic myocardial models, ranging from isotropic to orthotropic formulations, depending on the aim of the study. One of the most used approaches considers myocardial tissue as transversely isotropic [8–13]. For example, the model presented by Guccione et al. [14], one of the most common in this family, considers a unique direction of anisotropy along the muscular fiber direction. Other constitutive laws model the myocardium as orthotropic, following the aforementioned local 'fiber-sheet-normal' directions presented by LeGrice. Several studies use this formulation [15–19], being those presented by Costa et al. [20] and Holzapfel & Ogden [21] two of the most used.

To obtain the parameters that appear in these numerical models, two different approaches have been followed: using directly the results from *in vitro* mechanical tests on biopsied tissue samples, or, alternatively, obtaining *in vivo* properties from medical imaging. Within the first option, the most standard approach nowadays characterizes the mechanical response of the cardiac tissue from biaxial, or triaxial shear extension tests, or both test types together. Planar biaxial extension tests have been performed on parallel-to-the-epicardium sheets of myocardial tissue of different animal species [22–27], showing a highly nonlinear and transversely isotropic response of the cardiac tissue. Alternatively, triaxial shear experiments have been carried out [28], demonstrating an orthotropic behavior following the LeGrice FSN directions. Recent experiments have been also performed combining biaxial and triaxial shear data [29], where the orthotropic behavior of the tissue was once again demonstrated. Other novel possibility is combining single shear and pure shear stress tests [30].

All these methods are however destructive and require invasive surgery. Thus, other alternatives based on non-invasive *in vivo* measurements and inverse analysis have been proposed to characterize the cardiac tissue. This approach involves the formulation and solution of a multi-step non-linear optimization problem, which, together with the high correlation between the constitutive parameters, limits its applicability to transversely isotropic models, such as Guccione's [14]. Following this line, Augenstein et al. [8,31] proposed a finite element-based inverse analysis to reproduce myocardium strain and stress distributions in porcine hearts. This FE model was based on Diffusion Tensor Magnetic Resonance Images (DTMRI) and pressure recordings in ex vivo passive ventricular inflation experiments. Wang et al. [11] also developed an inverse methodology using *in vivo* MR images combined with ex vivo DTI for a canine model. Xi et al. [12] used a reduced-order unscented Kalman filter to optimize the mechanical parameters for a human heart. Rumindo et al. [13] proposed a patient-specific inverse methodology based on the experimentally observed volume by MRI and the end-diastolic pressure-volume relationship (EDPVR) established by Klotz et al. [32]. They validated the obtained parameters by several LV physiological function metrics. All these studies used Guccione's law for myocardium characterization and, although cardiac tissue has already been proved to present an orthotropic response, few studies have been performed for orthotropic material models. Remme et al. [18] estimated the parameters for the pole-zero law [33], but only 3 material parameters were estimated. Gao et al. [17] presented an inverse analysis for the obtention of the Holzapfel & Ogden [21] complete set of mechanical parameters by validating the strain data and pressure–volume relationships, but they did not validate if their results reproduced the *in vitro* response.

Although many studies have been carried out in these two lines, to the best of our knowledge, it has not been analyzed whether the results obtained from both are compatible. With respect to the *in vitro* characterization, the existing studies are only focused on getting experimental properties, but do not analyze the feasibility of the derived parameters in heart numerical models or their ability to reproduce the *in vivo* response. Other works, centered on numerical studies, use those *in vitro* properties, but they stress the need for their prior readjustment to reproduce the physiological behavior of the tissue [34], or they lead to results that are far from accurately simulating the actual *in vivo* function [35].

On the other hand, *in vivo* studies directly derive their properties from images and medical data, obtaining patient-specific solutions that may be influenced by various factors such as inter-patient variability or accuracy of data collection. Furthermore, in this second methodology, no explicit characterization is performed for pure deformation modes, and they do not assess if their results are able to reproduce the experimental behavior reported from *in vitro* studies.

Moreover, we must be especially aware that, due to the complex behavior of cardiac tissue, structurally-based constitutive models, especially orthotropic ones, usually include many parameters with some of them closely correlated, while some other having little impact on the overall heart functional response [17,36]. This means that several combinations of parameters may provide a similar and apparently acceptable reproduction of our specific experimental data but are unable to get a realistic *in vivo* behavior. This problem has been widely mentioned [8,11,15,17,20,36], suggesting the need for using as much data as available to get a sufficiently robust constitutive model.

Following this last line of thinking, we propose in this work a methodology that combines data from *in vitro* mechanical tests and from *in vivo* MRI and hemodynamics to obtain the mechanical properties of a particular material model. Our aim is to demonstrate that using this combined set of data permits reproducing both the *in vitro* tests performed in our laboratory, and, at the same time, the *in vivo* heart behavior, thus assessing whether the *in vitro* parameters are suitable for *in silico* simulation of *in vivo* cardiac mechanical function. To this end, we have used experimental results from biaxial and triaxial shear tests on porcine cardiac tissue samples, as well as *in vivo* pressure-volume (PV) relationships by means of the conductance catheter method (CCM) and magnetic resonance imaging (MRI). Finally, a parameter identification method is proposed that uses finite element modeling to simulate the ventricular hemodynamic response. Then, a two-step minimization approach is used in which we firstly obtain the mechanical parameters from the *in vitro* mechanical data, while in a second stage the *in vitro* properties are modified to simultaneously reproduce the *in vitro* and *in vivo* response (Fig. 1).

2. Mechanical properties estimation by *in vitro* experimental data

2.1. Experimental characterization of porcine tissue

Porcine left ventricular biopsy specimens were obtained from 7 white pigs (Sus scrofa domesticus) of 18-22 weeks of age (weight between 55–65 kg) at the Experimental Surgery Service of the Aragon Health Sciences Institute. All animal experiments complied with the regulations of the local animal welfare committee for the care and use of experimental animals and were approved by local authorities (Ethics Committee on Animal Experimentation, CEAEA, of the University of Zaragoza). All animal procedures conformed to the guidelines from Directive 2010/63/EU of the European Parliament on the protection of animals used for scientific purposes.

Biaxial and triaxial shear testing were performed following the protocol presented by Sommer et al. [29]. Very briefly, 25x25 mm parallel-to-the-epicardium biaxial samples were obtained at different wall thickness levels. Samples were cut alongside the local main fiber direction and the cross fiber direction, which corresponds to the FN plane according to LeGrice FSN coordinate system. For shear testing, 4 mm cubic samples were obtained. Samples were also aligned with the FSN axis, obtaining 6 different shear modes according to Dokos et al. [28] (FN-FS-SF-SN-NF-NS). Both tests were performed at different strain levels under quasistatic conditions to neglect viscoelastic effects. We performed a total of 16 biaxial tests and 51 triaxial shear tests. In the present study, only 20% strain biaxial results and positive 50% shear results were considered for parameter obtention. At the biaxial characterization, 5 different loading ratios were applied between the Main Fiber Direction (MFD, corresponding to the F LeGrice orientation)

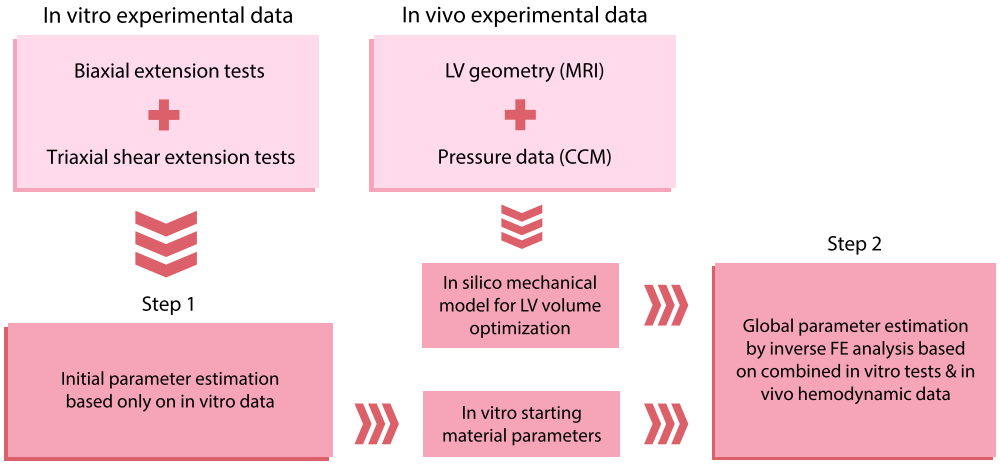

Fig. 1. Workflow of the proposed method to determine the mechanical parameters: i) Mechanical tests into *in vitro* samples, ii) *in vivo* LV data obtention (diastolic pressure gradient and initial geometry), iii) LV FE model implementation and iv) two-steps combined optimization for mechanical parameters identification.

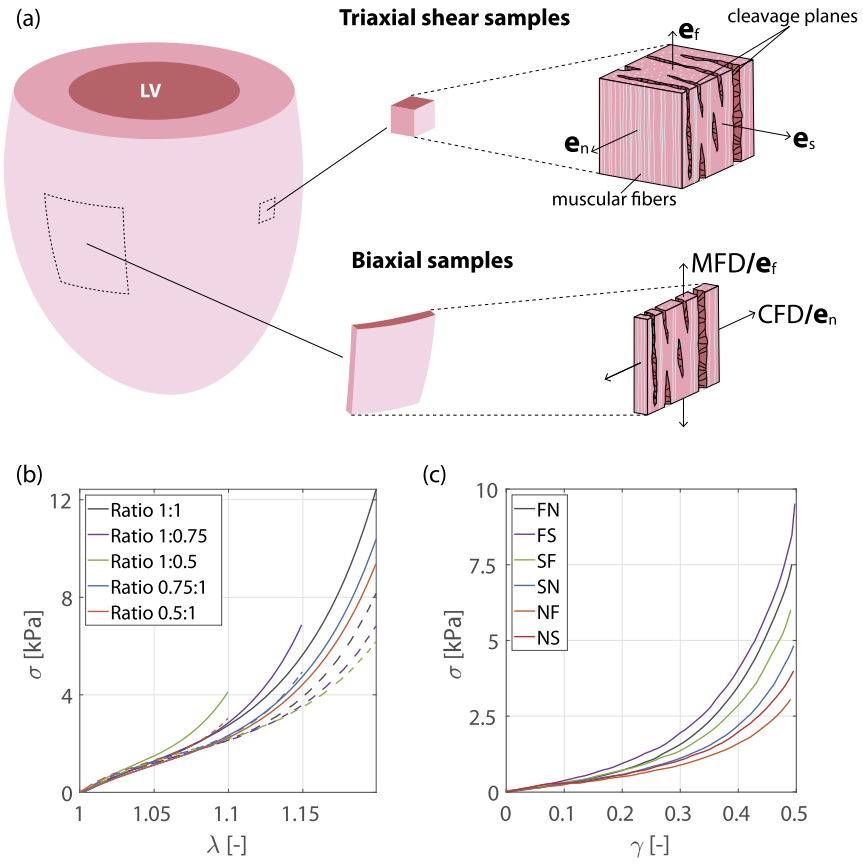

Fig. 2. Experimental protocol summary. a) Scheme of the sample obtention procedure. Biaxial and triaxial shear samples were obtained aligned with the FSN directions. b) Considered biaxial extension tests mean results at 20% of deformation (continuous lines correspond to MFD and dotted lines correspond to CFD). c) Considered triaxial shear results at 50% of shear strain.

and the Cross Fiber Direction (CFD, corresponding to the N LeGrice orientation), 1(MFD):1(CFD)-1:0.75-1:0.5-0.75:1-0.5:1. For more detailed information, the reader is referred to Sommer et al. (2015) [29,37]. Fig. 2 shows a summary of the experimental conditions and the main results is shown.

2.2. Myocardium constitutive model

For the formulation of a constitutive law that reproduces the myocardial behavior, we have considered the tissue as orthotropic, hyperelastic and incompressible. To ensure an accurate reproduction of the experimental behavior, two widely used material models have been contrasted, the invariant-based version of the Costa model [20] and the Holzapfel & Ogden (HO) model [21]. Following the classic notation, we can define the deformation of a certain body as the motion of its points from their reference configuration, $\Omega_0 \subset \mathbb{R}^3$, to their current-state positions, $\Omega_t \subset \mathbb{R}^3$. Hence, we can define the relative motion of any point of the reference domain, $\mathbf{X} \in \Omega_0$, by the current coordinates $\mathbf{x}(\mathbf{X}, t)$. The deformation gradient is then defined as $\mathbf{F} = \nabla_{\mathbf{X}}\mathbf{x}$, and its determinant, $J = det(\mathbf{F}) > 0$ ($J = 1$ for incompressible materials). Finally, the strain is

described by the right Cauchy Green tensor, $\mathbf{C} = \mathbf{F}^T\mathbf{F}$. The stress-strain relationship in a hyperelastic material is given by the strain energy density function (SEDF), ϕ, representing the stored elastic energy per unit volume. At the present study, the SEDF will be expressed as function of the invariants of $\mathbf{C}$, defined as

$$I_1 = \mathbf{C} : \mathbf{I}, \qquad I_2 = det(\mathbf{C})\mathbf{C}^{-1} : \mathbf{I}, \qquad I_3 = det(\mathbf{C}) = J. \tag{1}$$

For an orthotropic material as the myocardium, the anisotropic pseudo-invariants along the microstructural directions, which in our case correspond to the fiber-sheet-normal axes are usually used. These pseudo-invariants represent the squared stretch along these directions, and are therefore defined as

$$I_{ff} = \mathbf{C} : \mathbf{e}_f \otimes \mathbf{e}_f, \qquad I_{ss} = \mathbf{C} : \mathbf{e}_s \otimes \mathbf{e}_s, \qquad I_{nn} = \mathbf{C} : \mathbf{e}_n \otimes \mathbf{e}_n, \tag{2}$$

where $\mathbf{e}_k$ ($k \in \{f, s, n\}$) denote the unitary vectors in each direction. Likewise, the coupling pseudo-invariants between the microstructural directions, are expressed as

$$I_{fs} = \mathbf{C} : \mathbf{e}_f \otimes \mathbf{e}_s, \qquad I_{fn} = \mathbf{C} : \mathbf{e}_f \otimes \mathbf{e}_n, \qquad I_{sn} = \mathbf{C} : \mathbf{e}_s \otimes \mathbf{e}_n. \tag{3}$$

Costa's model [20] considers an orthotropic formulation of the exponential Fung-type law and it is normally formulated in terms of the rotated Green Lagrange strain tensor. However, as presented by Nordsletten et al. [15], we can also obtain its formulation in terms of the invariants of the right Cauchy Green strain tensor as follows (IBC formulation)

$$\phi = \frac{C}{4}[exp(Q(\mathbf{C})) - 1] + p(J-1), \qquad Q(\mathbf{C}) = \sum_{kl \in R_{IBC}} b_{kl}(I_{kl} - \delta_{kl})^2, \tag{4}$$

where $R_{IBC} = [ff, ss, nn, fs, fn, sn]$ and δ_{kl} denotes the Kronecker delta. The IBC model thus depends on a total of 7 parameters, an external scaling constant, C, and 6 anisotropy parameters, b_{kl}. The second Piola Kirchhoff stress tensor can be obtained from its expression in terms of the invariants

$$\mathbf{S} = \sum_{kl \in R} 2\frac{\partial \phi}{\partial I_{kl}} sym(\mathbf{e}_k \otimes \mathbf{e}_l) + pJ\mathbf{C}^{-1}, \tag{5}$$

where $sym(\mathbf{X}) = \frac{1}{2}(\mathbf{X} + \mathbf{X}^T)$ represents the symmetric part of a given tensor. Finally, the first Piola Kirchhoff (PK1) and Cauchy stress tensors can be obtained through the standard weighted push forward operations ($\mathbf{P} = \mathbf{FS}$ and $\boldsymbol{\sigma} = J^{-1}\mathbf{FSF}^T$, respectively). The obtention of the analytical solution of the IBC model particularized for biaxial and simple shear extension tests can be found in Appendix A.

For the HO model, the SDEF is characterized by the following expression

$$\phi(\mathbf{C}) = \phi_{iso}(I_1) + \sum_{kl \in R_{HO}} \phi_{kl}(I_{kl}) + p(J-1), \tag{6}$$

where $R_{HO} = [ff, ss, fs]$ and

$$\phi_{iso}(I_1) = \frac{a}{2b}[exp(b(I_1 - 3)) - 1], \tag{7}$$

$$I_{kl} = \frac{a_{kl}}{2b_{kl}}[exp(b_{kl}(I_{kl} - \delta_{kl})^2) - 1]. \tag{8}$$

The HO model thus depends on a total of 8 parameters. Analogously to Eq. (5), the second Piola-Kirchhoff stress tensor is given by

$$\mathbf{S} = 2\frac{\partial \phi_{iso}}{\partial I_1}\mathbf{I} + \sum_{kl \in R_{HO}} 2\frac{\partial \phi_{kl}}{\partial I_{kl}} sym(\mathbf{e}_k \otimes \mathbf{e}_l) + pJ\mathbf{C}^{-1}. \tag{9}$$

Both the IBC and HO models have similar formulations, presenting each of them pros and cons for parameter estimation. The main differences are: (i) the IBC model strain-energy terms are coupled in a single exponential function, while the HO function is presented as a sum of different exponentials; (ii) the IBC model also includes *nn*, *fn* and *sn* strain modes; and (iii) the HO model includes an isotropic term which represents the stiffening of the extracellular matrix. Regarding (ii), it has been already presented in Li et al. [36] an extended version of the HO model (HOE) which hypothesizes that the myocardium exhibits further modes of coupling than the ones considered by the I_{fs} and includes the two other I_{kl} pseudo-invariants in Eq. (3). It should be mentioned that these additional terms were originally proposed by Holzapfel and Ogden [21] but they were ultimately excluded. With the addition of these terms Eqs. (10) and (11) result as

$$\phi(\mathbf{C}) = \phi_{iso}(I_1) + \sum_{kl \in R_{HOE}} \phi_{kl}(I_{kl}) + p(J-1), \tag{10}$$

$$\mathbf{S} = 2\frac{\partial \phi_{iso}}{\partial I_1}\mathbf{I} + \sum_{kl \in R_{HOE}} 2\frac{\partial \phi_{kl}}{\partial I_{kl}} sym(\mathbf{e}_k \otimes \mathbf{e}_l) + pJ\mathbf{C}^{-1}, \tag{11}$$

where now $R_{HOE} = [ff, ss, fs, fn, sn]$. Li et al. [36] stated that the inclusion of these additional terms improved the fitting and predictive capability of the HO model when applied to simple and pure shear strains. However, including the additional I_{kl} terms implies to increase significantly the number of material parameters in the SEDF (8 parameters at HO versus 12 parameters at HOE).

3. Mechanical properties estimation by *in vivo-in silico* data

3.1. Left ventricle in vivo geometry

An *in vivo* left ventricle (LV) geometry was reconstructed from magnetic resonance (MR) images. They were performed on 3 different healthy porcine hearts. Crossbred domestic pigs of either gender (Sus scrofa, weight 20-25 kg, Animalium KU Leuven, Leuven, Belgium) were sedated using Telazol (tiletamine 4 mg/kg and zolazepam 4 mg/kg) (Zoletil100, Virbac Animal Health, Carros, France) and xylazine (2.5 mg/kg, Vexylan, CEVA Sante Animale, Brussels, Belgium) and subsequently anesthetized with intravenous propofol (3 mg/kg bolus injection, Diprivan, AstraZeneca, Brussels, Belgium) followed by 10 mg/kg/h continuous infusion and remifentanil (18 μg/kg/h, Ultiva, GSK, Genval, Belgium). Mechanical ventilation with a mixture of air and oxygen (1:1) at a tidal volume of 8-10 ml/kg was adjusted to maintain normocapnia and normoxia. Electrocardiogram, blood pressure and oxygen saturation were continuously monitored using the intensive cardiac monitor system (Siemens). Animal 2 was selected as a representative specimen for the LV geometry obtention due to the good quality of its MR images. Cardiac MRI was performed on a 3T system (TRIO-Tim, Siemens, Erlangen) during suspended respiration using electrocardiographic triggering and cardiac-dedicated surface coils. Global volume was assessed with cine MRI in the vertical and horizontal long and short axes, covering the complete LV using 6-mm thick slices, at rest and during dobutamine-induced stress. Myocardial fiber orientation was estimated using ex-vivo diffusion tensor distribution MRI.

The initial *in vivo* geometry was selected at early diastole, when pressure is lowest. The minimum pressure geometry was considered to be equivalent to the zero-pressure geometry (0P) since the pressure at this time-point is barely null (0.08 kPa, Fig. 3.a). At that instant, the LV cavity volume observed is 45 ml. For context, the volumes observed at end of systole (ES) and diastole (ED) were 34 and 75 ml, respectively. The 0P voxelized LV geometry was obtained by manually segmenting the early diastole frame of the cine cardiac MR sequence.

Initially, the LV segmentation was tetrahedralized with a mean edge length of 1.26 mm which resulted in a LV mesh of 64477 nodes and 345685 elements [38]. Moreover, a rule-based model was employed for defining the FSN cardiac fiber field of the LV mesh (Fig. 4.b-d), as reported in Bayer et al. (code version 2023.3.0) [39]. Briefly, the local longitudinal, circumferential and radial coordinated system was computed from a multi-diffusion analysis on the LV model. The longitudinal fiber direction F was determined by clockwise linearly rotating the local circumferential axis from 60 to -60 degrees from endo- to epicardium, respectively. A sensitivity analysis was carried out to study the influence of fiber distribution on the minimization process. In addition to

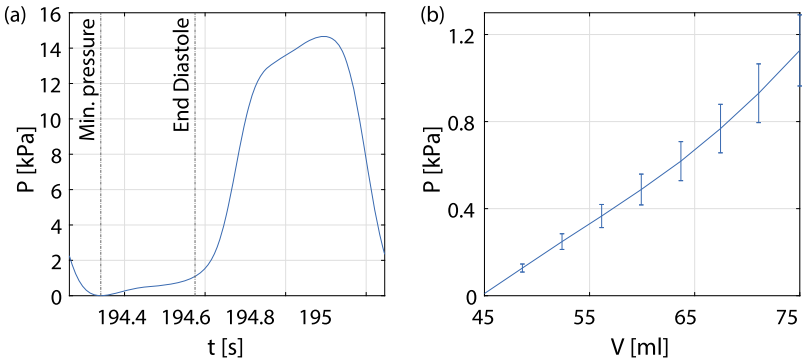

Fig. 3. CCM LV pressure recordings. a) Full cycle pressure gradient for a significant heartbeat. b) Strictly passive inflation mean pressure gradient considered in the simulations.

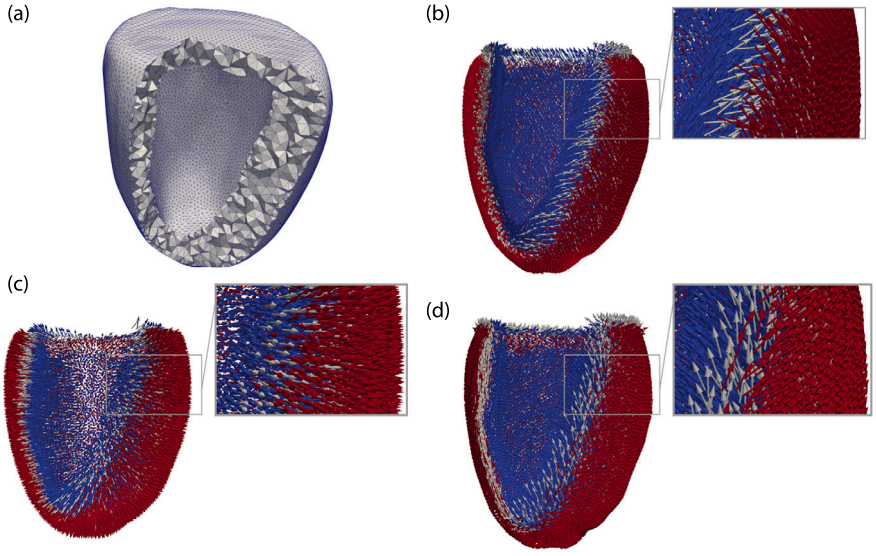

Fig. 4. Considered FE model geometry. a) Finite element mesh of the MRI *in vivo* geometry. b) Fiber field distribution for the F, c) S and d) N directions.

the -60º/60º orientation (endocardium/epicardium), the -50º/60º and -60º/50º cases were analyzed. Our methodology achieved a good fit for all the orientations considered, without any significant difference between the three cases (Supplementary data). The S direction was set as perfectly radial to the LV, while the N direction was defined as normal to the FS plane. Afterwards, in order to solve the numerical problem with the FE method, a coarser mesh was generated for the initial geometry, since the computational cost was too expensive with the original mesh size. A covered LV mesh of 107704 elements and 25504 nodes (mean tetrahedral edge length of 2.2 mm) was defined from the segmentation. Subsequently, the FSN fiber orientation in the covered LV mesh was interpolated from the uncovered thinner one employing radial basis functions. The final LV mesh and its fiber field can be observed in Fig. 4.a.

3.2. LV pressure-volume relationship

Diastolic inflation from the 0P to ED has been considered. The tissue was considered to present strictly passive behavior during this phase. For pressure gradient recordings, invasive hemodynamics was performed using a 5-French Millar equipment (Millar Instruments, Houston, TX, USA) for pressure-conductance catheter methodology (CCM), which was retrogradely introduced into the LV via carotid artery. dP/dt_{max} and dP/dt_{min} were recorded during steady state conditions. During the CCM experiment, a total of 118 heartbeats were recorded at the ventricular cavity. None of these beats corresponded to the MR images obtained, so the mean value of the 0P-ED pressure gradient was computed (Fig. 3.b). ED was identified thanks to the dP/dt recordings during the cycle, coinciding with the point at which the pressure starts to rise drastically.

3.3. Finite element model

A FE model was implemented using the software Abaqus (Abaqus 6.14.1, Symulia) considering the geometry and pressure gradient aforementioned. The recorded pressure was introduced as a boundary condition for the simulations and the 0P-ED volume increment due to this pressure gradient was used as one of the variables at the minimization process. C3D4H elements were used. Hybrid formulation is needed since the material is assumed to be incompressible. The mesh consists of a total of 25504 nodes and 107704 elements. UANISOHYPER subroutine was used for the implementation of the IBC material model. Fluid Cavity was implemented to control pressure volume conditions along ventricular inflation. For the Fluid Cavity condition, it is necessary to specify a closed surface, so extra elements were added on the top of the ventricular cavity. These elements are not considered for the mechanical analysis, they are only introduced to obtain a completely closed ventricular cavity. Finally, we also constrained the displacements at the top nodes of these extra elements to ensure the fixation of the model.

4. Combined *in vivo* - *in vitro* parameters optimization

For the estimation of the parameters of the selected material, we propose a minimization process with the aim of simultaneously re-

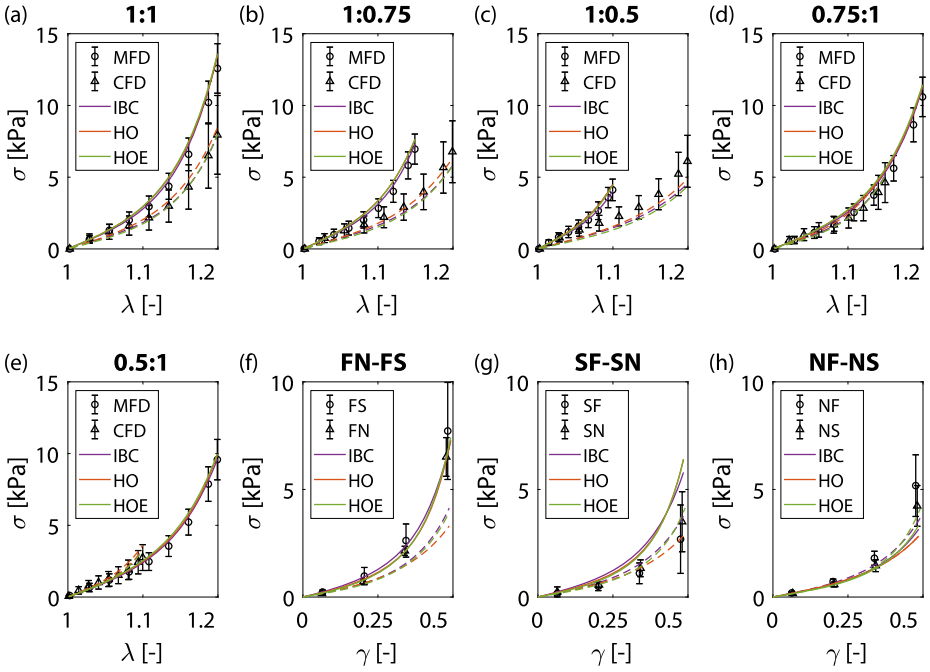

Fig. 5. Comparison of *in vitro* fitting for biaxial and triaxial shear extension tests with the considered constitutive models: Invariant-based Costa (IBM), Holzapfel & Ogden (HO) and Extended HO (HOE). Dotted lines correspond to the simulated results of the second experimental curve of each plot, which are CFD, FN, SN and NS, respectively.

producing both the *in vivo* PV data recorded in the CCM and MRI experiments and the results of the *in vitro* mechanical testing. To define the objective function of the minimization, we implemented the Mean Squared Error (MSE) between the simulated and the experimental results of the different inputs considered, which is defined as follows

$$f_{obj} = f_{tests} + f_{PV}, \tag{12}$$

$$f_{tests} = \frac{1}{k+1}\frac{1}{N_{tests}}\sum_{i=1}^{N_{tests}}\left(\sum_{i=1}^{N_{points}}\left(\frac{\mathbf{P}_{test}-\mathbf{P}_{an}}{max(\mathbf{P}_{test})}\right)^2\right), \tag{13}$$

$$f_{PV} = \frac{k}{k+1}\sum_{i=1}^{N_{points}}\left(\frac{V_{CCM}-V_{FEM}}{max(V_{CCM})}\right)^2, \tag{14}$$

where N_{points} corresponds to the number of points evaluated in each curve, which was fixed to 100 in every term; $\mathbf{P}_{test}$ and $\mathbf{P}_{an}$ represent the experimental and analytical values of the PK1 stress tensor for each strain mode test, respectively; N_{tests} is the total amount of considered *in vitro* tests for the fitting process, equal to 12; V_{CCM} and V_{FEM} are the volumes recorded along the passive filling in the MR images and the FE simulations, respectively. Finally, k corresponds to a weighting factor between the volume data and the experimental data, which was taken to be equal to 5 after a sensitivity analysis as described below. Errors were normalized by dividing them by the maximum experimental value, since the order of values and units of the PK1 stresses and the PV curves volumes are different. For the experimental minimization, the 6 different shear modes presented by Dokos et al. [28] as well as 3 different biaxial loading ratios (1:1-1:0.5-0.5:1) were considered. The resting 2 biaxial loading ratios (0.75:1-1:0.75) were used for validation of the obtained parameters, so they were not considered in the optimization process.

We considered two different stages for the optimization (Fig. 1). First, we obtained the parameters that reproduced only the *in vitro* mechanical response (taking f_{tests} as the objective function). Subsequently, these constants were used as the starting point for the next stage, where the overall response (f_{obj} as the objective function) was minimized. Therefore, in the first step, the minimization process only requires the *in vitro* data, so the initial set of constants is obtained without the need to perform numerical simulations. In the second step, in addition to the *in vitro* data, we used the FE model to inversely estimate the ED volume in each iteration, using the experimental PV data from the CCM and MRI. Thus, both *in vitro* and *in vivo* responses are taken into account in the second stage. The seven IBC material parameters were considered in both stages.

The minimization was conducted using the Matlab function *fmincon*, a gradient-based function for non-linear objective functions. Other studies have proposed the use of trust-region-reflective algorithms [17], genetic algorithms [40] or medium-scale algorithms such as sequential quadratic programming optimization techniques [8,31,11]. Gradient-based optimizations tend to be inefficient when the objective presents several local minima, as in our case. However, by imposing a sufficiently high initial step, *fmincon* was able to avoid local minima and eventually reach the global minimum of the problem. The interior-point algorithm has been selected as it is a large-scale algorithm that helps to reduce the computational cost [41–43].

Finally, to assess the goodness of fitting of the obtained results for both the *in vitro* and the *in vivo* data, we have considered the coefficient of determination, (R^2), which is defined as

$$R^2 = 1 - \frac{\sum_{i=1}^{N}(Y_i-\hat{Y})^2}{\sum_{i=1}^{N}(Y_i-\bar{Y})^2}, \tag{15}$$

where Y correspond to the experimental values considered for each test, $\hat{Y}$ to the simulated values, $\bar{Y}$ to the mean experimental value and N to the number of considered points

5. Results

5.1. In vitro fitting and material model selection

Firstly, we compare the three proposed material models, IBC, HO and HOE, to check their fitting and predictive capability against our experimental data. For this first analysis, only the data from the *in vitro* mechanical tests were used, not the PV diagrams. Fig. 5 shows the estimated Cauchy stress obtained for each model against the level

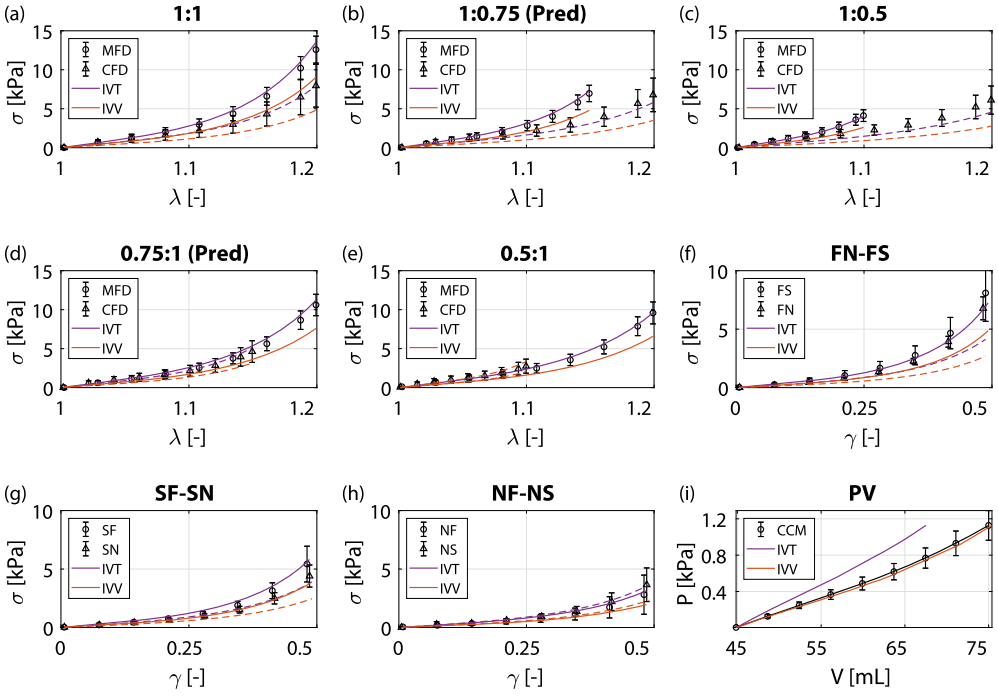

Fig. 6. Comparison of *in vitro* (a-h) and *in vivo* (i) data for the two initial approaches: Only *in vitro* tests were considered in the minimization process (IVT) and only *in vivo* passive inflation were considered in the minimization process (IVV). Dotted lines correspond to the simulated results of the second experimental curve of each plot, which are CFD, FN, SN and NS, respectively.

Table 1
Goodness of *in vitro* fitting values for different constitutive laws. Two different groups considered: Fit (Biaxial ratios 1-3-5 + Shear tests) and Pred (Biaxial ratios 2-4).

SEDF	R^2 (Fit)	R^2 (Pred)
ICB	0.9796	0.9836
HO	0.9564	0.9708
HOE	0.9830	0.9715

of stretch, for every considered strain mode. The goodness of fit for each of the models is shown in Table 1. To get a global value of R^2 for all the experimental curves, we estimated the individual values for each experiment and then computed their median term. All models obtain acceptable fits, staying within the experimental deviation range in practically all tests. The IBC and HOE models show the best results, being very similar to each other. If we analyze the results of Table 1 in greater detail, we see that the IBC model presents slightly better results for the prediction curves (ratios 2 and 4 of the biaxial tests) and the HOE model presents slightly better results for the fitting curves (rest of the biaxial tests and tangential tests).

In view of these results, we decided to use the IBC model for the minimization process, since it presents the best response together with HOE and requires fewer fitting parameters (7 parameters for IBC and 12 for HOE).

5.2. Separated fitting for in vivo and in vitro characterization

Once selected the constitutive law for the optimization process, we started by simulating the passive inflation with the initial parameters obtained from the *in vitro* results (IVT). We also performed a parallel study to obtain a set of parameters only from the *in vivo* passive inflation data (IVV), neglecting the IVT ones. The aim of this first process is to analyze whether the parameters obtained separately are comparable.

Fig. 6 shows the fittings for *in vitro* mechanical testing and the *in vivo* diastolic inflation for both scenarios. The results obtained for each of them are not entirely satisfactory, since they significantly mismatch their unconsidered counterpart. In the IVT case (only f_{tests} were considered), the PV adjustment is not accurate enough, obtaining lower end-diastolic volume (65 ml) than the MRI (75 ml), well outside the deviation range (Fig. 6.f). In the IVV case (only f_{PV} were considered), the fit of the experimental curves is also greatly affected. In Table 2, we show the IBC parameters and the different minimization errors for each case. It can be seen that the parameters are very different for IVT and IVV. For the IVV case, we even get non-physiological values for b_{ss} and b_{nn}, as we obtain a higher value for b_{nn} than b_{ss}, which would mean that the stiffness along the N direction is higher than the S direction. This behavior is in disagreement with what has been reported previously [28,29] and suggests that *in vivo* pressure-volume data is not enough to fully characterize the tissue response by itself. With respect to the minimization errors, the obtained values are lower for the IVT than for the IVV case. However, as already mentioned, the *in vivo* estimated volume for the IVT case is not sufficiently accurate.

Table 2 shows the final minimization errors, after applying the weighting factor, k. To estimate this factor, the original minimization errors were considered: $f^{IVT}_{tests,0} = 0.219$, $f^{IVT}_{PV,0} = 0.622$ and $f^{IVV}_{tests,0} = 3.324$, $f^{IVV}_{tests,0} = 0.067$. The ratio between these errors allows us to estimate k. For the IVT case, the estimated $f^{IVT}_{PV,0}$ value is 0.622, while in the IVV case, $f^{IVV}_{tests,0}$ is 3.324, which gives a ratio of approximately 5.34. In order for the minimization process to converge to a result capable of adjusting the physiological response without neglecting the fine-tuning of *in vitro* tests, it is necessary to prioritize the adjustment of the inflation volume. Therefore, a weighting factor of 5 was considered.

These results of the parallel analyses show that the parameters obtained when considering only the *in vitro* or the *in vivo* responses are substantially different from each other, suggesting that, apparently, it is not possible to simultaneously reproduce both responses. However, as we will see below, due to the multiplicity of solutions to the orthotropic problem, if we introduce both behaviors into the minimization process

Table 2
Invariant-based Costa model mechanical parameters and minimization MSE values for different fitting strategies.

	C [kPa]	b_{ff}	b_{ss}	b_{nn}	b_{fs}	b_{fn}	b_{sn}	f_{tests}	f_{PV}	f_{obj}
IVT	1.884	2.723	1.650	1.320	3.874	2.734	2.964	0.073	0.518	0.591
IVV	1.275	2.844	1.205	1.533	3.816	2.612	2.882	1.107	0.056	1.163
MIN	1.231	3.382	2.284	1.287	3.856	2.603	2.973	0.191	0.033	0.224

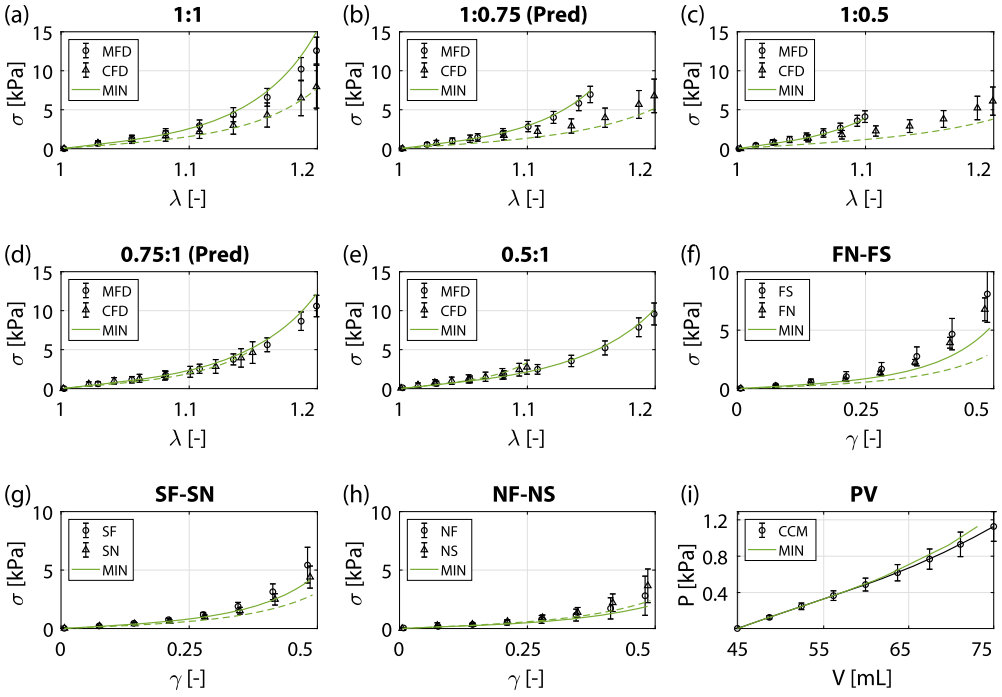

Fig. 7. Comparison of *in vitro* (a-h) and *in vivo* (i) fitting for the obtained parameters after the minimization process (MIN). Dotted lines correspond to the simulated results of the second experimental curve of each plot, which are CFD, FN, SN and NS, respectively.

it is possible to arrive at a set of parameters that satisfies both requirements at the same time.

5.3. In vitro and in vivo combined fitting and parameter estimation

Table 2 and Fig. 7 present the results after the proposed minimization process (MIN), considering $k = 5$. The material parameters obtained are intermediate between the IVT and IVV cases as well as the minimization errors. In Table 3, we include R^2 values for each of these three scenarios. The errors are divided in three different groups of curves: the *in vitro* fitting curves (triaxial shear tests and biaxial ratios 1:1, 1:0.5, 0.5:1), FIT, *in vitro* prediction curves (0.75:1, 1:0.75), PRED, and the *in vivo* pressure-volume curve, PV. Both Fig. 7 and Table 3 reflect the impossibility of achieving a simultaneous adjustment of the hemodynamic response and *in vitro* assays if both datasets are not considered in the minimization process. However, the MIN group achieves a reasonably acceptable, although not perfect, simultaneous fit. Results in Fig. 7 are around the range of deviation in almost all curves, except for biaxial ratio 3 and FS-FN tests, which are the worst fitted in all scenarios. In this case, despite achieving a reasonable adjustment of the hemodynamic response, the b_{ss} and b_{nn} constants do reach physiological values in contrast to the IVV case. MIN values for R^2 in each group show that, after the minimization process, a reliable reproduction of all the input data is achieved, without obtaining any R^2 value lower than 0.85.

Finally, Fig. 8 shows the deformed ventricular geometry and the maximum principal strain distribution at ED for each case. As expected, the strains achieved for IVV and MIN are larger than those for IVT, since

Table 3
Goodness of fitted values for different fitting strategies. Three different groups considered: Fit (Biaxial ratios 1-3-5 + Shear tests), Pred (Biaxial ratios 2-4) and PV (*in vivo* PV curve).

	R^2 (Fit)	R^2 (Pred)	R^2 (PV)
IVT	0.977	0.984	0.697
IVV	0.687	0.717	0.995
MIN	0.815	0.962	0.992

the volume reached at the end of the simulation is larger in those scenarios (Fig. 6-7). Nevertheless, the strain maps seem to follow the same pattern for the two cases, suggesting that the distribution of local deformations along the ventricular wall is similar for the different selected properties in each case.

6. Discussion

6.1. Material model selection

Both IBC and HO are the most used orthotropic material models for the characterization of the passive mechanical behavior of the myocardium. Although they share very similar formulations, there are minor differences between them that lead to variations in their predictive capability. Nordsletten et al. [15] noted that the IBC model has greater predictive capability when applied to biaxial stretching at different loading ratios, whereby the HO one fails to predict different stretches at cross-fiber directions under non-equibiaxial loads. This is

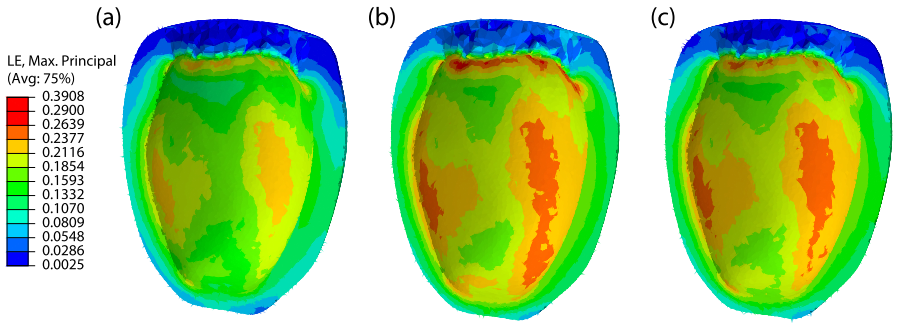

Fig. 8. Comparison of the maximum principal strain for the simulated End Diastole (ED) geometries: a) *In vitro* data properties (IVT) only, b) *In vivo* data properties (IVV) only, c) Combined data properties (MIN).

due to the approach followed by each model to relate the deformations associated with each strain mode. In the IBC model, all modes are coupled within the same exponential term, achieving an inherent coupling between the microstructural directions. On the other hand, the HO model considers each strain mode in separate terms, which neglects the interaction between the orthotropy directions in non-equibiaxial biaxial tests. This study also highlights that the HO model has a better predictive ability for highly non-linear responses compared to the IBC one. Li et al. [36] also stated that the HO model fails to predict multiaxial loading paths such as pure shear testing. The HOE model was proposed as a solution to these limitations since it offers advantages when fitting multiaxial loading paths.

All these same comments are reflected in the obtained results. First, given that our tests are largely composed of non-equibiaxial biaxial tests, the IBC model presents a slightly better prediction than the HO one. Closer results to experiments were achieved by the HOE approach when compared to the HO one. Special attention should be paid to analyze which constitutive law best fits each specific problem, and both Costa and HO models offer great predictive power. However, in our particular problem, the IBC one offers the best response in relation to the number of parameters and the fitting accuracy. It should also be noted that this initial conclusion is highly dependent on the particular experimental dataset.

6.2. *In vitro & in vivo combined minimization process*

The use of *in vitro* properties for *in vivo* simulations of cardiac response has sometimes been questioned since the effect of tissue disruption during sample obtention is not well understood [17,20]. However, *in vitro* characterization is still of great interest nowadays and there are many works that base their models on *in vitro* properties, considering different alternatives for their implementation. For example, there are studies [15,29,30,36] that use *in vitro* studies only to validate their proposed numerical or experimental methodologies, since *in vitro* testing allows to analyze the tissue response to pure strain modes, not as in physiological conditions when heart is subjected to coupled strain modes during the cardiac cycle. Other studies by Bovendeerd et al. [9,34,44] use *in vitro* biaxial tests by Yin et al. [23] in their FE models, but they tune some of the mechanical parameters so that the simulated hemodynamic response agrees reasonably with *in vivo* results [34], without checking if the *in vitro* response is still respected with that new parameter set. On the other hand, in the work published by Göktepe et al. [35,45], the passive response is based exclusively on the *in vitro* shear properties presented in Dokos et al. [28] to simulate the PV heart cycle. However, the inflation obtained is significantly smaller than the physiological one [35], suggesting that the considered material is not representative of the *in vivo* behavior. Hence, none of these studies have succeeded to implement *in vitro* properties directly to accurately reproduce the *in vivo* hemodynamic response.

Therefore, the methodology presented proposes an alternative to use the *in vitro* properties while ensuring that the physiological behavior is respected in subsequent simulations. We have shown that using this novel approach is possible to get an acceptable *in vivo* and *in vitro* fitting for an orthotropic material model as the IBC one. We believe that this methodology can be very useful for the development of computational models using *in vitro* properties and we think that this is justified by the high correlation between the parameters of the IBC model, which leads to multiple parametric solutions that match the same experimental results with sufficient accuracy. Our methodology overcomes this problem, offering one of that family of parametric solutions that is able to accurately reproduce the *in vivo* behavior.

With respect to the works that use *in vivo* properties derived from clinical images, very few of them consider orthotropic models [17,18]. The non-uniqueness of the solution, as well as the limited amount of available *in vivo* input data, make very expensive to obtain a representative set of parameters for this highly multi-parametric type of constitutive laws. That is why most studies use simpler transversely isotropic materials [8,10–13,16]. Incorporating *in vitro* results in the parameter identification problem can help in guiding the process and facilitate the search for a unique solution. In addition, this new approach is also an interesting alternative when insufficiently accurate *in vivo* data is available. This methodology allows us to obtain patient-specific physiological properties only from hemodynamic data, complementing them with our own species-specific *in vitro* data or those from literature.

Although we have shown promising results, there are some limitations in this study that need to be addressed. First, we did not validate the distribution of local deformations along the wall, since we did not have this type of data. It would be necessary to analyze whether the proposed solutions not only reproduce the global hemodynamic response but also the local strains in the myocardium. Second, we have focused this first analysis only on passive behavior, but it would be of interest to analyze the entire cardiac cycle including the active contraction stage. Lastly, we have not performed a comprehensive study on the influence of different sets of *in vivo* data on our methodology, which may be interesting for our study. In future research, we should move towards a more patient-specific approach considering different MRI and hemodynamic data alternatives. Furthermore, throughout this study we have considered several assumptions that may have an impact on the results and should be taken into account.

First, we have considered the myocardium to be purely hyperelastic, neglecting its viscoelastic response. This is fairly standard, as the time scale of the cardiac cycle is much shorter than the relaxation characteristic time of the heart tissue [21]. However, this assumption has been recently challenged, as novel studies have been presented in which the myocardium is considered as a visco-hyperelastic material [15,19], claiming that the viscoelastic part of the mechanical response does have a significant influence on the overall behavior, and should be considered. The same applies to the compressibility of the tissue. We have considered the cardiac tissue to be fully incompressible, as it is normally assumed. Nevertheless, recently, some studies have also questioned this hypothesis considering the myocardium as a material with a non-negligible compressibility [46] or even considering a variable com-

pressibility during the cycle depending on the blood perfusion of the heart wall [16,30]. It should be also noted that the initial pressure at the 0P geometry has been neglected since it is close to zero, but whether this hypothesis can have an impact on the process should be further explored. Finally, although a real patient-specific geometry has been used for the simulations, an idealized fiber field has been considered, without including phenomena such as dispersion or cross-linking between parallel fibers. There are studies that insist on the importance of these phenomena on the cardiac tissue behavior [9]. However, no data were available to us to introduce a more realistic fiber distribution.

7. Conclusions

A new approach has been proposed aiming at healthy myocardium mechanical parameter estimation using an orthotropic hyperelastic constitutive law. We have proposed a minimization process that combines *in vitro* and *in vivo* results to ensure a robust set of parameters that simultaneously reproduces both responses. The proposed methodology has proven its capacity to reproduce the *in vivo* tissue response from *in vitro* data, at least at the hemodynamic level. We believe that this approach can help in the development of computational models as it simplifies the process of fitting highly complex material models by including the *in vitro* data and, in addition, helps to shed some light on the relationship between the *in vitro* and *in vivo* tissue response.

Declaration of competing interest

The authors declare no conflicts of interest.

Data availability

Data will be made available on request.

Acknowledgements

This work is supported by the European Economic Community through research project BRAV3, C1-BHC-07-2019, H2020; the Next Generations fund of the Spanish Ministry of Science and Innovation through the Cardioprint Project, PLEC2021-008127 and the Spanish Ministry of Economy and Competitiveness through research project PID2019-107517RB-I003. The authors gratefully acknowledge research support from the ICTS “NANBIOSIS”, specifically by the Tissue & Scaffold Characterization Unit (U13) of the CIBER in Bioengineering, Biomaterials & Nanomedicne (CIBER-BBN at the University of Zaragoza). CIBER Actions are financed by the Instituto de Salud Carlos III with assistance from the European Regional Development Fund. Authors would also like to acknowledge A. Latorre for his great help in the development of the computational environment and K. Jansens from Eindhoven University of Technology (TU/e) for his help in processing the *in vivo* experimental data.

Appendix A. *In vitro* tests analytical solution

Here we describe the full procedure to obtain the IBC constitutive law analytical solution, both for biaxial and triaxial shear extension tests.

A.1. Biaxial extension tests

Considering a biaxial extension test as shown in Fig. 2.a, we can define the deformation gradient tensor, **F**, as

$$\mathbf{F}=\begin{pmatrix}\lambda_f & 0 & 0\\ 0 & \lambda_s & 0\\ 0 & 0 & \lambda_n\end{pmatrix}=\begin{pmatrix}\lambda_f & 0 & 0\\ 0 & \frac{1}{\lambda_f\lambda_n} & 0\\ 0 & 0 & \lambda_n\end{pmatrix}, \tag{A.1}$$

where λ_f, λ_s and λ_n are the respective elongation in the LeGrice directions F, S and N. Since we have considered the myocardium as incompressible, we can rewrite the tensor F as in the second term of Equation (A.1). Then, as described in Section 2.2, we can define the right Cauchy-Green tensor, **C**, as

$$\mathbf{C}=\begin{pmatrix}\lambda_f^2 & 0 & 0\\ 0 & \frac{1}{\lambda_f^2\lambda_n^2} & 0\\ 0 & 0 & \lambda_n^2\end{pmatrix}. \tag{A.2}$$

According to Eq. (5) we can write the PK2 tensor, **S**, as

$$\begin{aligned}\mathbf{S}&=\begin{pmatrix}2\frac{\partial\phi}{\partial I_{ff}} & \frac{\partial\phi}{\partial I_{fs}} & \frac{\partial\phi}{\partial I_{fn}}\\ \frac{\partial\phi}{\partial I_{fs}} & 2\frac{\partial\phi}{\partial I_{ss}} & \frac{\partial\phi}{\partial I_{sn}}\\ \frac{\partial\phi}{\partial I_{fn}} & \frac{\partial\phi}{\partial I_{sn}} & 2\frac{\partial\phi}{\partial I_{ff}}\end{pmatrix}+pJ\mathbf{C}^{-1}\\ &=\begin{pmatrix}2\frac{\partial\phi}{\partial I_{ff}}+\frac{p}{\lambda_f^2} & \frac{\partial\phi}{\partial I_{fs}} & \frac{\partial\phi}{\partial I_{fn}}\\ \frac{\partial\phi}{\partial I_{fs}} & 2\frac{\partial\phi}{\partial I_{ss}}+p\lambda_f^2\lambda_n^2 & \frac{\partial\phi}{\partial I_{sn}}\\ \frac{\partial\phi}{\partial I_{fn}} & \frac{\partial\phi}{\partial I_{sn}} & 2\frac{\partial\phi}{\partial I_{ff}}+\frac{p}{\lambda_n^2}\end{pmatrix}.\end{aligned} \tag{A.3}$$

The Cauchy stress tensor can be obtained by $\boldsymbol{\sigma}=J^{-1}\mathbf{F}\mathbf{S}\mathbf{F}^T$, resulting in

$$\boldsymbol{\sigma}=C\cdot e^{Q_{Bx}}\begin{pmatrix}b_{ff}\lambda_f^2(\lambda_f^2-1) & 0 & 0\\ 0 & \frac{b_{ss}\left(\frac{1}{\lambda_f^2\lambda_n^2}-1\right)}{\lambda_f^2\lambda_n^2} & 0\\ 0 & 0 & b_{nn}\lambda_n^2(\lambda_n^2-1)\end{pmatrix}+p, \tag{A.4}$$

where

$$e^{Q_{Bx}}=e^{\left(b_{ff}\left(\lambda_f^2-1\right)^2+b_{ss}\left(\frac{1}{\lambda_f^2\lambda_n^2}-1\right)^2+b_{nn}\left(\lambda_n^2-1\right)^2\right)} \tag{A.5}$$

To obtain p, we can impose $\sigma_{ss}=0$. Finally, we need to obtain the PK1 tensor by $\mathbf{P}=\mathbf{F}\mathbf{S}$, since is the stress tensor implemented at the minimization process. The final expressions for P_{ff} and P_{nn} are

$$\begin{aligned}P_{ff}&=\left[b_{ff}(\lambda_f^2-1)-b_{ss}\frac{\left(\frac{1}{\lambda_f^2\lambda_n^2}-1\right)}{\lambda_f^4\lambda_n^2}\right]\\ &\times C\cdot\lambda_f\cdot e^{\left(b_{ff}\left(\lambda_f^2-1\right)^2+b_{ss}\left(\frac{1}{\lambda_f^2\lambda_n^2}-1\right)^2+b_{nn}\left(\lambda_n^2-1\right)^2\right)}\end{aligned} \tag{A.6}$$

$$\begin{aligned}P_{nn}&=\left[b_{nn}(\lambda_n^2-1)-b_{ss}\frac{\left(\frac{1}{\lambda_f^2\lambda_n^2}-1\right)}{\lambda_f^2\lambda_n^4}\right]\\ &\times C\cdot\lambda_n\cdot e^{\left(b_{ff}\left(\lambda_f^2-1\right)^2+b_{ss}\left(\frac{1}{\lambda_f^2\lambda_n^2}-1\right)^2+b_{nn}\left(\lambda_n^2-1\right)^2\right)}\end{aligned} \tag{A.7}$$

A.2. Triaxial shear extension test

Considering now a simple shear extension test as shown in Fig. 2.a, we can now define the deformation gradient, **F**, as

$$\mathbf{F}=\begin{pmatrix}1 & 0 & 0\\ \gamma & 1 & 0\\ 0 & 0 & 1\end{pmatrix}. \tag{A.8}$$

It should be noted that, depending on the shear direction with respect to the different tissue's orthotropy orientations, there are a total of 6 different simple shear stress configurations as stated by Dokos et al.

[28]. In this Appendix, we will focus only on the FS mode, which corresponds to a shear stress in the FS plane where the loading direction is the S-direction, according to Holzapfel & Ogden [21]. Once again, we can now define the right Cauchy-Green tensor, as

$$\mathbf{C} = \begin{pmatrix} \gamma^2+1 & \gamma & 0 \\ \gamma & 1 & 0 \\ 0 & 0 & 1 \end{pmatrix}. \tag{A.9}$$

According to Eq. (5), for simple shear we can write the PK2 tensor now as

$$\mathbf{S} = \begin{pmatrix} 2\frac{\partial \phi}{\partial I_{ff}} + p & \frac{\partial \phi}{\partial I_{fs}} - p\gamma & \frac{\partial \phi}{\partial I_{fn}} \\ \frac{\partial \phi}{\partial I_{fs}} - p\gamma & 2\frac{\partial \phi}{\partial I_{ss}} + p(\gamma^2+1) & \frac{\partial \phi}{\partial I_{sn}} \\ \frac{\partial \phi}{\partial I_{fn}} & \frac{\partial \phi}{\partial I_{sn}} & 2\frac{\partial \phi}{\partial I_{ff}} + p \end{pmatrix}, \tag{A.10}$$

and the Cauchy stress tensor as

$$\boldsymbol{\sigma} = \begin{pmatrix} p+\gamma^2 b_{ff} \cdot C e^{Q_{Sh}} & \left(\gamma^2 b_{ff} + \frac{b_{fs}}{2}\right)\gamma C e^{Q_{Sh}} & 0 \\ \left(\gamma^2 b_{ff} + \frac{b_{fs}}{2}\right)\gamma C e^{Q_{Sh}} & \left(\gamma^3 b_{ff} + \frac{b_{fs}(\gamma+1)}{2}\right)\gamma C e^{Q_{Sh}} + p(\gamma^2-\gamma+1) & 0 \\ 0 & 0 & p \end{pmatrix}, \tag{A.11}$$

where

$$e^{Q_{Sh}} = e^{\left(b_{ff}\cdot\gamma^4 + b_{fs}\cdot\gamma^2\right)}. \tag{A.12}$$

Now, to obtain p, we impose $\sigma_{nn} = 0$. From Eq. (A.11), we observe directly $p = 0$. Finally, the PK1 tensor term P_{fs} is given by

$$P_{fs} = \left(\gamma^2 \cdot b_{ff} + \frac{b_{fs}}{2}\right) \cdot \gamma \cdot C \cdot e^{\left(b_{ff}\cdot\gamma^4 + b_{fs}\cdot\gamma^2\right)}. \tag{A.13}$$

Repeating this process for the other 5 shear strain modes, we can express the respective terms of the PK1 tensor as

$$P_{sf} = \left(\gamma^2 \cdot b_{ss} + \frac{b_{fs}}{2}\right) \cdot \gamma \cdot C \cdot e^{\left(b_{ss}\cdot\gamma^4 + b_{fs}\cdot\gamma^2\right)}, \tag{A.14}$$

$$P_{ns} = \left(\gamma^2 \cdot b_{nn} + \frac{b_{sn}}{2}\right) \cdot \gamma \cdot C \cdot e^{\left(b_{nn}\cdot\gamma^4 + b_{sn}\cdot\gamma^2\right)}, \tag{A.15}$$

$$P_{sn} = \left(\gamma^2 \cdot b_{ss} + \frac{b_{sn}}{2}\right) \cdot \gamma \cdot C \cdot e^{\left(b_{ss}\cdot\gamma^4 + b_{sn}\cdot\gamma^2\right)}, \tag{A.16}$$

$$P_{nf} = \left(\gamma^2 \cdot b_{nn} + \frac{b_{fn}}{2}\right) \cdot \gamma \cdot C \cdot e^{\left(b_{nn}\cdot\gamma^4 + b_{fn}\cdot\gamma^2\right)}, \tag{A.17}$$

$$P_{fn} = \left(\gamma^2 \cdot b_{ff} + \frac{b_{fn}}{2}\right) \cdot \gamma \cdot C \cdot e^{\left(b_{ff}\cdot\gamma^4 + b_{fn}\cdot\gamma^2\right)}. \tag{A.18}$$

However, as proved by Latorre & Montans [47], only five out of the six different simple shear responses in preferred planes, are independent. As they can be related by

$$\sigma_{fs} - \sigma_{sf} + \sigma_{sn} - \sigma_{ns} + \sigma_{nf} - \sigma_{fn} = 0. \tag{A.19}$$

In equations (A.13)-(A.18) we can see that the parameters of the IBC model are coupled to each other in the shear modes. As we have mentioned throughout the study, this makes obtaining a single solution to the mechanical problem very complex and opens the possibility of various combinations of parameters to be able to reproduce the same experimental response.

Appendix B. Supplementary material

Supplementary material related to this article can be found online at https://doi.org/10.1016/j.compstruc.2023.107241.

References

[1] Zile MR, Baicu CF, Gaasch WH. Diastolic heart failure abnormalities in active relaxation and passive stiffness of the left ventricle. N Engl J Med 2004;350(19):1953–9.
[2] Fomovsky GM, Holmes JW. Evolution of scar structure, mechanics, and ventricular function after myocardial infarction in the rat. Am J Physiol, Heart Circ Physiol 2010;298(1):H221–8.
[3] Chabiniok R, Wang VY, Hadjicharalambous M, Asner L, Lee J, Sermesant M, et al. Multiphysics and multiscale modelling, data–model fusion and integration of organ physiology in the clinic: ventricular cardiac mechanics. Interface Focus 2016;6(2):20150083.
[4] Streeter Jr DD, Spotnitz HM, Patel DP, Ross Jr J, Sonnenblick EH. Fiber orientation in the canine left ventricle during diastole and systole. Circ Res 1969;24(3):339–47.
[5] LeGrice IJ, Smaill B, Chai L, Edgar S, Gavin J, Hunter PJ. Laminar structure of the heart: ventricular myocyte arrangement and connective tissue architecture in the dog. Am J Physiol, Heart Circ Physiol 1995;269(2):H571–82.
[6] Legrice, Smaill. Extended confocal microscopy of myocardial laminae and collagen network. J Microsc 1998;192(2):139–50.
[7] Fomovsky GM, Thomopoulos S, Holmes JW. Contribution of extracellular matrix to the mechanical properties of the heart. J Mol Cell Cardiol 2010;48(3):490–6.
[8] Augenstein KF, Cowan BR, LeGrice IJ, Nielsen PM, Young AA. Method and apparatus for soft tissue material parameter estimation using tissue tagged magnetic resonance imaging. J Biomech Eng 2005;127(1):148–57.
[9] Bovendeerd PH, Kroon W, Delhaas T. Determinants of left ventricular shear strain. Am J Physiol, Heart Circ Physiol 2009;297(3):H1058–68.
[10] Genet M, Lee LC, Nguyen R, Haraldsson H, Acevedo-Bolton G, Zhang Z, et al. Distribution of normal human left ventricular myofiber stress at end diastole and end systole: a target for in silico design of heart failure treatments. J Appl Physiol 2014;117(2):142–52.
[11] Wang VY, Lam H, Ennis DB, Cowan BR, Young AA, Nash MP. Modelling passive diastolic mechanics with quantitative MRI of cardiac structure and function. Med Image Anal 2009;13(5):773–84.
[12] Xi J, Lamata P, Lee J, Moireau P, Chapelle D, Smith N. Myocardial transversely isotropic material parameter estimation from in-silico measurements based on a reduced-order unscented Kalman filter. J Mech Behav Biomed Mater 2011;4(7):1090–102.
[13] Rumindo GK, Ohayon J, Croisille P, Clarysse P. In vivo estimation of normal left ventricular stiffness and contractility based on routine cine MR acquisition. Med Eng Phys 2020;85:16–26.
[14] Guccione JM, McCulloch AD, Waldman LK. Passive material properties of intact ventricular myocardium determined from a cylindrical model. J Biomech Eng 1991;113(1):42–55.
[15] Nordsletten D, Capilnasiu A, Zhang W, Wittgenstein A, Hadjicharalambous M, Sommer G, et al. A viscoelastic model for human myocardium. Acta Biomater 2021;135:441–57.
[16] Liu H, Soares JS, Walmsley J, Li DS, Raut S, Avazmohammadi R, et al. The impact of myocardial compressibility on organ-level simulations of the normal and infarcted heart. Sci Rep 2021;11(1):1–15.
[17] Gao H, Li W, Cai L, Berry C, Luo X. Parameter estimation in a Holzapfel–Ogden law for healthy myocardium. J Eng Math 2015;95:231–48.
[18] Remme EW, Hunter PJ, Smiseth O, Stevens C, Rabben SI, Skulstad H, et al. Development of an in vivo method for determining material properties of passive myocardium. J Biomech 2004;37(5):669–78.
[19] Zhang W, Jilberto J, Sommer G, Sacks MS, Holzapfel GA, Nordsletten DA. Simulating hyperelasticity and fractional viscoelasticity in the human heart. Comput Methods Appl Mech Eng 2023;411:116048.
[20] Costa KD, Holmes JW, McCulloch AD. Modelling cardiac mechanical properties in three dimensions. Philos Trans R Soc Lond, Ser A, Math Phys Eng Sci 2001;359(1783):1233–50.
[21] Holzapfel GA, Ogden RW. On planar biaxial tests for anisotropic nonlinearly elastic solids. a continuum mechanical framework. Math Mech Solids 2009;14(5):474–89.
[22] Demer LL, Yin F. Passive biaxial mechanical properties of isolated canine myocardium. J Physiol 1983;339(1):615–30.
[23] Yin FC, Strumpf RK, Chew PH, Zeger SL. Quantification of the mechanical properties of noncontracting canine myocardium under simultaneous biaxial loading. J Biomech 1987;20(6):577–89.
[24] Humphrey JD, Strumpf RK, Yin FCP. Determination of a constitutive relation for passive myocardium: I. A new functional form. J Biomech Eng 1990;112(3):333–9.
[25] Sacks MS, Chuong CJ. Biaxial mechanical properties of passive right ventricular free wall myocardium. J Biomech Eng 1993;115(2):202–5.
[26] Novak VP, Yin F, Humphrey J. Regional mechanical properties of passive myocardium. J Biomech 1994;27(4):403–12.
[27] Hill MR, Simon MA, Valdez-Jasso D, Zhang W, Champion HC, Sacks MS. Structural and mechanical adaptations of right ventricle free wall myocardium to pressure overload. Ann Biomed Eng 2014;42(12):2451–65.
[28] Dokos S, Smaill BH, Young AA, LeGrice IJ. Shear properties of passive ventricular myocardium. Am J Physiol, Heart Circ Physiol 2002;283(6):H2650–9.
[29] Sommer G, Schriefl AJ, Andrä M, Sacherer M, Viertler C, Wolinski H, et al. Biomechanical properties and microstructure of human ventricular myocardium. Acta Biomater 2015;24:172–92.

[30] Avazmohammadi R, Li DS, Leahy T, Shih E, Soares JS, Gorman JH, et al. An integrated inverse model-experimental approach to determine soft tissue three-dimensional constitutive parameters: application to post-infarcted myocardium. Biomech Model Mechanobiol 2018;17(1):31–53.
[31] Augenstein KF, Cowan BR, LeGrice IJ, Young AA. Estimation of cardiac hyperelastic material properties from MRI tissue tagging and diffusion tensor imaging. In: Medical image computing and computer-assisted intervention–MICCAI 2006: 9th international conference, proceedings, part I, vol. 9. Springer Berlin Heidelberg; 2006. p. 628–35.
[32] Klotz S, Hay I, Dickstein ML, Yi G-H, Wang J, Maurer MS, et al. Single-beat estimation of end-diastolic pressure-volume relationship: a novel method with potential for noninvasive application. Am J Physiol, Heart Circ Physiol 2006;291(1):H403–12.
[33] Nash MP, Hunter PJ. Computational mechanics of the heart. J Elast 2000;61:113–41.
[34] Bovendeerd P, Arts T, Huyghe J, Van Campen D, Reneman R. Dependence of local left ventricular wall mechanics on myocardial fiber orientation: a model study. J Biomech 1992;25(10):1129–40.
[35] Göktepe S, Acharya S, Wong J, Kuhl E. Computational modeling of passive myocardium. Int J Numer Methods Biomed Eng 2011;27(1):1–12.
[36] Li DS, Avazmohammadi R, Merchant SS, Kawamura T, Hsu EW, Gorman III JH, et al. Insights into the passive mechanical behavior of left ventricular myocardium using a robust constitutive model based on full 3d kinematics. J Mech Behav Biomed Mater 2020;103:103508.
[37] Sommer G, Haspinger DC, Andrä M, Sacherer M, Viertler C, Regitnig P, et al. Quantification of shear deformations and corresponding stresses in the biaxially tested human myocardium. Ann Biomed Eng 2015;43(10):2334–48.
[38] Si H. TetGen, a Delaunay-based quality tetrahedral mesh generator. ACM Trans Math Softw 2015;41(2):1–36.
[39] Bayer JD, Blake RC, Plank G, Trayanova NA. A novel rule-based algorithm for assigning myocardial fiber orientation to computational heart models. Ann Biomed Eng 2012;40(10):2243–54.
[40] Nair AU, Taggart DG, Vetter FJ. Optimizing cardiac material parameters with a genetic algorithm. J Biomech 2007;40(7):1646–50.
[41] Byrd RH, Gilbert JC, Nocedal J. A trust region method based on interior point techniques for nonlinear programming. Math Program 2000;89:149–85.
[42] Coleman TF, Li Y. On the convergence of interior-reflective Newton methods for nonlinear minimization subject to bounds. Math Program 1994;67(1–3):189–224.
[43] Waltz RA, Morales JL, Nocedal J, Orban D. An interior algorithm for nonlinear optimization that combines line search and trust region steps. Math Program 2006;107(3):391–408.
[44] Bovendeerd P, Huyghe J, Arts T, Van Campen D, Reneman R. Influence of endocardial-epicardial crossover of muscle fibers on left ventricular wall mechanics. J Biomech 1994;27(7):941–51.
[45] Berberoğlu E, Göktepe S. Computational modeling of myocardial infarction. Proc IUTAM 2015;12:52–61.
[46] McEvoy E, Holzapfel GA, McGarry P. Compressibility and anisotropy of the ventricular myocardium: experimental analysis and microstructural modeling. J Biomech Eng 2018;140(8).
[47] Latorre M, Montáns FJ. Wypiwyg hyperelasticity without inversion formula: application to passive ventricular myocardium. Comput Struct 2017;185:47–58.